



Unraveling the dominance of intrinsic catalytic activities over electrical properties in electrocatalytic performance of two-dimensional chromium chalcogenide nanosheets

Jiefu Yang^{a,1}, Mei Zheng^{a,1}, Yao Wu^{a,1}, Frédéric Le Goualher^{a,1}, Jun Di^b, Teddy Salim^{a,c}, Ya Deng^a, Chao Zhu^a, Shasha Guo^a, Bijun Tang^a, Shuzhou Li^{a,*}, Zheng Liu^{a,d,e,**}

^a School of Materials Science & Engineering, Nanyang Technological University, Singapore 639798, Singapore

^b School of Chemistry and Chemical Engineering, National Special Superfine Powder Engineering Research Center, Nanjing University of Science and Technology, Nanjing 210094, China

^c Facility for Analysis, Characterization, Testing and Simulation (FACTS), Nanyang Technological University, Singapore 639798, Singapore

^d School of Electrical and Electronic Engineering & The Photonics Institute, Nanyang Technological University, Singapore 639798, Singapore

^e CINTRA CNRS/NTU/THALES, UMI 3288, Research Techno Plaza, Singapore, Singapore

ARTICLE INFO

Keywords:

Two-dimensional electrocatalysts
Intrinsic catalytic activity
Electrical properties
Hydrogen evolution reaction

ABSTRACT

In this study, we synthesized a new category of materials, 2D Cr₂X₃ (where X = S, Se, and Te), using an APCVD method. By leveraging the same space group and identical exposed facets of the as-synthesized Cr₂X₃ nanoflakes, we compared their catalytic performance for HER and electrical properties to unveil the contribution of electrical conductivity in the overall performance. A descending trend in HER activities from Cr₂S₃ to Cr₂Se₃, and Cr₂Te₃ was found, as evidenced by the increasing overpotentials and decreasing current densities at the same overpotential. Interestingly, electrical properties showed an improving trend from Cr₂S₃ to Cr₂Se₃, and Cr₂Te₃, as revealed by I_{DS}-V_G and I_{DS}-V_{DS} tests based on FET devices, respectively. The primary factor affecting overall catalytic performance was found to be intrinsic catalytic activities rather than electrical properties, as supported by DFT calculations. These insights emphasize that the focus of harnessing intrinsic catalytic activities when exploring 2D electrocatalysts.

1. Introduction

Electrocatalysis has garnered significant academic interest due to its crucial role in diverse fields, such as renewable energy conversion, environmental protection, and chemical synthesis [1–3]. Identifying an optimal electrocatalyst necessitates thorough consideration of various essential perspectives that govern electrocatalytic activities. Among these factors, the material's intrinsic catalytic properties stand as a fundamental determinant of its ability to facilitate desired chemical transformations. Additionally, electrical conductivities also play a critical role in ensuring facile electron transport within the catalyst and modulating the electron distribution [4–6]. A synergetic interplay of both factors shapes the overall effectiveness of an electrocatalyst, driving researchers to explore materials that optimize these perspectives

and pave the way for groundbreaking advancements in electrocatalytic applications.

Despite extensive research in the field of electrocatalysis, a significant gap persists in effectively distinguishing the individual contributions of intrinsic catalytic activity and electrical conductivity to the overall electrocatalytic performance. The significance of a material's electrical conductivity often goes unnoticed in conventional electrocatalysts, as they are commonly prepared in powder form and dispersed on a conductive matrix or substrate. To address this limitation, utilizing 2D materials with on-chip microelectrodes offers a promising system to reveal the impact of electrical conductivity. By using pristine 2D nanosheets as the sole catalyst without interference from additional conductive components, it becomes possible to better understand the role of electrical conductivity in the reaction. Nonetheless, challenges

* Corresponding author.

** Corresponding author at: School of Materials Science & Engineering, Nanyang Technological University, Singapore 639798, Singapore.

E-mail addresses: LISZ@ntu.edu.sg (S. Li), z.liu@ntu.edu.sg (Z. Liu).

¹ These authors contributed equally to this work.

persist due to various undesirable variables originating from different compositions, phases, or exposed facets of the materials. Thus, selecting a suitable material class for standardized comparison and mechanism exploration remains a challenge.

In this work, a class Cr_2X_3 ($\text{X} = \text{S}, \text{Se}, \text{Te}$) nanosheets with uniform thickness (~ 8 nm) have been synthesized using an ambient pressure chemical vapor deposition method. Their identical Cr-to-chalcogen atom ratio, uniform space group of $P\text{-}31c$ and the same exposed facets render them adequate material models for both electrocatalytic and electrical transport characterization. A customized on-chip microelectrode test has revealed a decreasing trend in HER activities under acidic conditions from Cr_2S_3 , to Cr_2Se , and Cr_2Te_3 considering the onset potentials and current densities at fixed overpotential. However, the electrical transport test based on field-effect transistor devices manifested an opposing trend as the electrical properties. Density Functional Theory (DFT) was later utilized to demonstrate how intrinsic catalytic activities are a more dominant factor, as compared to the electrical properties, for HER performances in this material class.

2. Experimental and calculation

2.1. Synthesis of 2D chromium chalcogenides nanosheets (Cr_2X_3)

The sample was prepared by an ambient pressure chemical vapor deposition (APCVD) method. Around 10 mg mixed powder of anhydrous CrCl_3 ($\geq 98.0\%$, Aldrich) and NaCl (ACS reagent, $\geq 99.0\%$ Aldrich) in a mass ratio of 10:1 was placed inside a ceramic boat, with a $20 \times 10 \times 0.2$ mm fluorophlogopite mica ($\text{KMg}_3\text{AlSi}_3\text{O}_{10}(\text{F}, \text{OH})_2$) placed in an inclined layout over the precursor mixture. A quartz boat containing 100 mg of elemental chalcogen powders ($\text{S}, \text{Se}, \text{Te}$) was placed at the upstream position with various distances to the furnace center to realize different localized temperatures at the boat tip to make sure the chalcogen boat temperature was set at about 150°C , 250°C , and 450°C for S, Se , and Te , respectively. After chemical loading, the quartz tube was flushed with 500 sccm dry and high-purity Ar gas for 20 min to remove residue air and moisture. Next, carrier gas flow of 120-sccm Ar and 20-sccm H_2 was introduced throughout the entire synthesis process. The furnace temperature was ramped up to 750°C at a rate of $50^\circ\text{C}/\text{min}$ and then maintained for 3 min. For Cr_2S_3 , the growth temperature was slightly lowered to 720°C due to the speedy nucleation rate at higher temperatures would lead to dense yet undesired small nanoflakes [7]. The system was then quickly cooled to room temperature with the assistance of an electric fan. The as-grown nanosheets were immediately protected by two layers of poly(methyl methacrylate) (PMMA A7 950, Microchem), which each was prepared via spin coating at 3000 rpm and 2-min baking at 120°C for 2 min.

2.2. Characterization of 2D chromium chalcogenides nanosheets (Cr_2X_3)

The surface topology analysis utilized optic images captured with Olympus BX53M Industrial Microscopes. The physical dimensions of crystal flakes were measured using the Olympus software. To determine the sample thickness, atomic force microscopy (AFM) was carried out on the Asylum Research Cypher Scanning Probe Microscope system in near-contact mode. Raman spectra were acquired using a Witec CRM200 confocal Raman microscopy system, with excitation at 532 nm. X-ray photoelectron spectroscopy (XPS) analysis was performed on an AXIS Supra spectrometer (Kratos Analytical, UK) equipped with a hemispherical analyzer and a monochromatic Al K-alpha source (1487 eV) operated at 15 mA and 15 kV. The XPS spectra were obtained from a $700 \times 300 \mu\text{m}^2$ area with a take-off angle of 90° , using pass energies of 160 eV and 20 eV for survey and high-resolution scans, respectively. A 3.1-volt bias was applied to neutralize charge buildup on the sample surface. The binding energies (BEs) were charge-corrected based on the C 1s of adventitious carbon at 284.8 eV. For atomic resolution high-angle annular dark-field scanning transmission electron microscope

(HAADF-STEM) imaging, an aberration-corrected JEOL ARM-200CF (S) TEM equipped with a cold field emission gun and an Advanced STEM Corrector (ASCOR) probe corrector was used, operating at 200 kV. The beam convergence semi-angle was set to 28 mrad, and the HAADF collection angle ranged from 65 to 280 mrad. Energy-dispersive X-ray spectroscopy (EDX) data were collected using an Oxford X-Max TLE 100 mm^2 windowless SDD detector.

2.3. Electrocatalytic activity measurement based on microcell device

First, a Cr/Au bottom electrode matrix with 36 pads was prepared on a SiO_2/Si wafer by lithography using MicroWriter ML-3 laser writer and metal deposition using Kurt J. Lesker Nano Thermal Evaporator. Next, the protected 2D Cr_2X_3 nanosheets on the mica substrate were lifted off in deionized water with aid from both the surface tension of water and mechanical exfoliation enforced by tweezers. The PMMA layer with samples was later transferred to the bottom electrodes of the previously prepared chip. After 15-min baking at 120°C , PMMA was dissolved using acetone. Later, the whole chip was passivated by two layers of PMMA using the method described above. Areas of interest were then defined by electron beam lithography (EBL) (Nova nanoSEM 230 with digital pattern generator Nabity-NPGS). After soaking the microchip in MIBK/IPA (in a mass ratio of 1:3) to dissolve away the exposed PMMA, unprotected reaction windows were created, ready for subsequent electrocatalytic tests.

The HER performance was tested on a customized platform using a three-electrode system which consists of a high-purity graphite electrode as a counter electrode, an Ag/AgCl micro reference electrode (Harvard Apparatus), and a working electrode, established via a needle contact to the Au/Cr electrode. The 0.5 M H_2SO_4 electrolyte was applied in the form of solution droplets covering the reaction window and submerging both the counter and reference electrode tips.

2.4. Electrical characterization based on metal-oxide-semiconductor field-effect transistor (MOSFET)

Using the same PMMA coating and transferring techniques described above, samples were prepared on a SiO_2/Si substrate. Metal contacts (5 nm Cr/80 nm Au) were prepared using the above-mentioned lithography and metal deposition methods. The electrical properties of the FET device fabricated were measured in the MicroXact Probe Station by Primarius FS-Pro Semiconductor Device Parameter Analyzer.

2.5. Computational methods

Structural optimization of material models was performed via spin-polarized DFT using the Vienna ab initio Simulation Package (VASP) with the projector augmented wave (PAW) method [8–10]. The Perdew-Burke-Ernzerhof (PBE) generalized gradient approximation (GGA) was used to describe exchange-correlation energy [11]. The $\text{Cr}_2\text{S}_3(001)$, $\text{Cr}_2\text{Se}_3(001)$, and $\text{Cr}_2\text{Te}_3(001)$ surfaces were constructed using a 2×2 supercell with 2 at. layers. A vacuum space of 15 \AA was implemented to avoid electronic interactions between vertically neighboring cells. For the calculation details, the topmost layer was allowed to relax until the total energy changes fell below 1×10^{-5} eV per atom and the force exerted on each atom was smaller than 0.02 eV/\AA , while the bottommost layer was constrained to maintain the bulk crystal structure. A cutoff energy of 500 eV was utilized to expand the wave functions while the Brillouin zone was sampled with a $1 \times 1 \times 1$ Monkhorst-Pack mesh of k points [12]. A DFT-D3 empirical correction was adopted to describe the dispersion interaction [13].

Furthermore, the Gibbs free energy change (ΔG) was calculated by the following equation [14]:

$$\Delta G = \Delta E + \Delta E_{\text{ZPE}} - T\Delta S + eU + \Delta G_{\text{pH}}.$$

where ΔE is the electronic energy difference obtained from DFT calculations. The ΔE_{ZPE} and ΔS are changes of zero-point energies and entropy at 298.15 K, respectively, which are derived from the vibrational frequency. Notably, the vibrational frequency is calculated only for adsorbed hydrogen while the substrate was fixed. The entropy of the H_2 molecules was taken from the standard thermodynamic database. The e and U are the number of electrons transferred and the electrode potential. ΔG_{pH} is the free energy correction of pH, which can be calculated as $\Delta G_{\text{pH}} = k_{\text{B}}T \times \text{pH} \times \ln 10$. In our work, this term was neglected since the pH value is zero under the 0.5 M H_2SO_4 condition.

3. Results and discussion

3.1. Facile synthesis of ultrathin chromium chalcogenides nanosheets

Three types of Cr_2X_3 ($\text{X} = \text{S}, \text{Se}, \text{and Te}$) nanosheets were grown on freshly cleaved fluorophlogopite mica substrate at either 720 or 750 °C using CrCl_3 and relevant elemental chalcogens as described in the **Experimental** section. The low partial pressure of the chalcogen vapor supply was ensured by carefully monitoring and controlling the tip

distance of the chalcogen boat. Different chalcogen boats containing distinct chalcogen powders were positioned at varying locations based on their melting points, marked by the blue square in Fig. 1a. As the temperature approached the designated growth temperature, a small amount of hydrogen was introduced with the carrier gas to generate reductive hydrogen chalcogenides (H_2X) in the environment, which reacted with CrCl_3 to form Cr_2X_3 . [15]. Mica substrates were placed at an inclined inside the substrate boat, with CrCl_3 placed below the substrate as demonstrated in the red square. This setup led to a vapor pressure gradient of CrCl_3 at different locations near the mica substrate, resulting in samples with different thicknesses being produced in a single run, enabling easy preparation of ultrathin nanosheets. Thinner products tended to appear at regions (Fig. S1) further from the chlorides, as the lower supply of reactants promoted adatom migration on the chemically inert surfaces of the mica substrate, facilitating the subsequent epitaxial growth of Cr_2X_3 [16]. Notably, the thickness of Cr_2X_3 could be controlled by changing the growth duration as demonstrated in Fig. S2. Shorter growth time favors the growth of thinner sample, however at the expense of smaller dimensions and poorer coverage of the mica substrate. The as-synthesized Cr_2X_3 , for example, Cr_2S_3 nanosheets, could

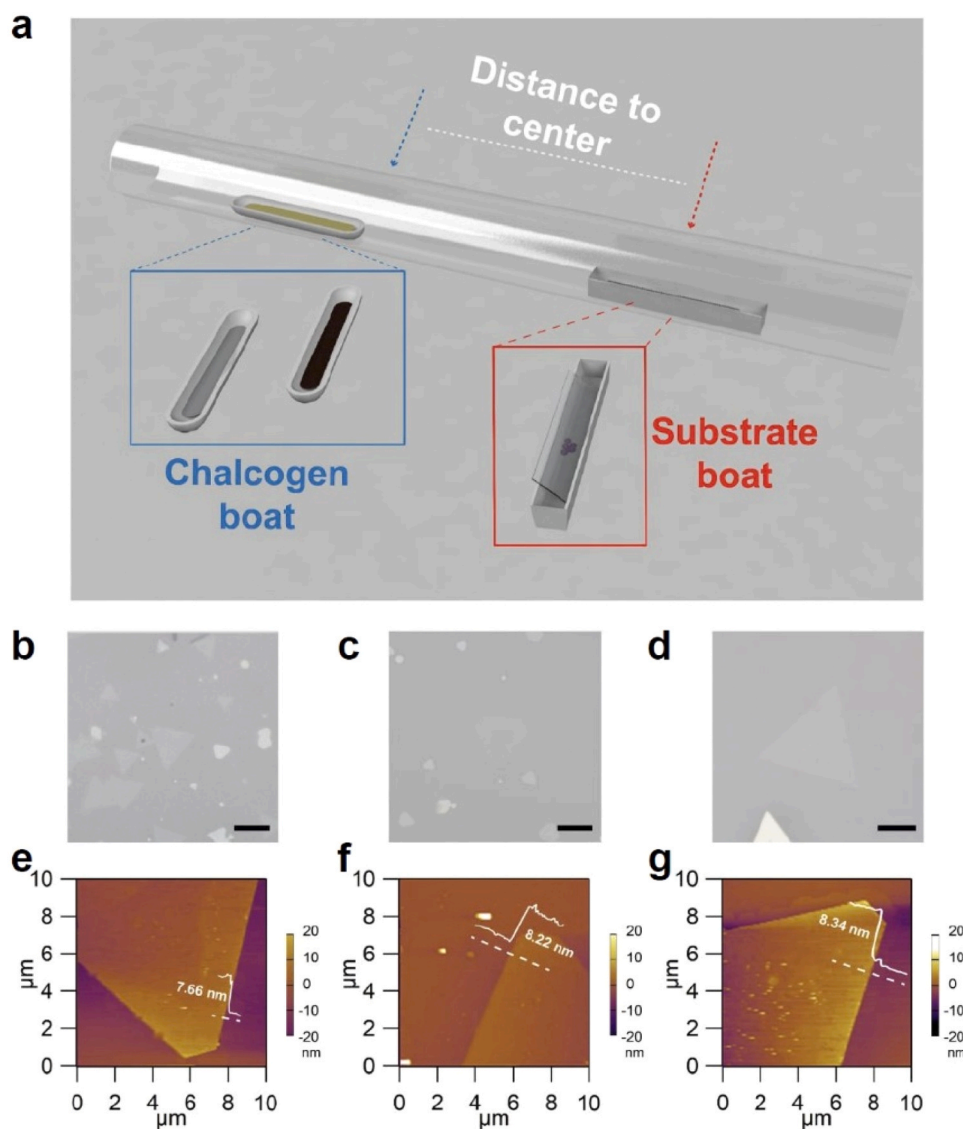


Fig. 1. (a) Chemical vapor deposition setup (CVD) and details for the preparation of Cr_2X_3 nanosheets. OM images of ultrathin (b) Cr_2S_3 , (c) Cr_2Se_3 , and (d) Cr_2Te_3 nanosheets. Scale bar: 20 μm . AFM images of ultrathin single (e) Cr_2S_3 , (f) Cr_2Se_3 , and (g) Cr_2Te_3 nanosheets. Insets indicate the height profile along the white dashed lines.

reach a thickness as low as about 6 nm (Fig. S3). However, the focus of the research was not to achieve the synthesis of atomically thin nanosheets, but rather to prepare robust nanosheets with sufficient dimensions for subsequent device fabrication and characterization of electrocatalytic properties. For consistency and practical purposes, a thickness of approximately 8 nm was chosen for all three species of nanosheets. Such nanosheets typically exhibit edge lengths exceeding 20 μm for Cr_2S_3 and Cr_2Se_3 (Fig. 1b,c), and around 50 μm for Cr_2Te_3 (Fig. 1d), as observed in the optical microscopic images. These nanosheets display characteristic morphologies, including triangles, truncated triangles, and hexagons, indicating the inherited three-fold or six-fold symmetries of the top facet. The similarity in macroscopic shapes suggests potentially identical surface atomic arrangements, supported by the predicted space groups of the three thermodynamically stable species, $P\bar{3}1c$ (No. 163) [17–19]. Further evidence will be presented in the structural analysis in subsequent sections.

The as-synthesized Cr_2S_3 , Cr_2Se_3 , and Cr_2Te_3 nanosheets exhibit smooth and flat surface finishes, as confirmed by atomic force microscopic images (Fig. 1e–g), with thicknesses close to 7.66 nm, 8.22 nm, and 8.34 nm, respectively. Nanosheets used for subsequent electrocatalytic, and electrical property characterization were selected based on their close thicknesses, which were determined by optical contrast.

For practical purposes, nanosheets grown on mica with a thickness lower than this value would hardly be perceptible to the unaided eye or under an optical microscope. Therefore, our choice of nanosheet thickness ensures visibility and justifies the selection of model materials for the study.

3.2. Compositional analysis of the ultrathin chromium chalcogenides (Cr_2X_3)

To preliminarily disclose the compositional information of the as-synthesized Cr_2X_3 nanosheets, individual nanosheets grown on mica substrates were analyzed using Raman spectroscopy with an excitation wavelength of 532 nm (Fig. 2a–c). It is important to note that while the Raman modes of the trigonal phase for Cr_2S_3 and Cr_2Se_3 under the same laser conditions were not reported in previous research, similarities in Raman shifts were observed from crystals with similar structures, supporting the claimed compositions of Cr_2S_3 and Cr_2Se_3 . For Cr_2S_3 (Fig. 2a), two primary peaks at 251.1 cm^{-1} and 283.8 cm^{-1} were identified, along with two less intense peaks (at 170.3 cm^{-1} and 345.7 cm^{-1}) barely distinguished from the nearby peaks of mica substrate (indicated by green lines). Since the proposed structures of Cr_2X_3 are considered 2D layers of 1 T- CrX_2 stacking right above each other

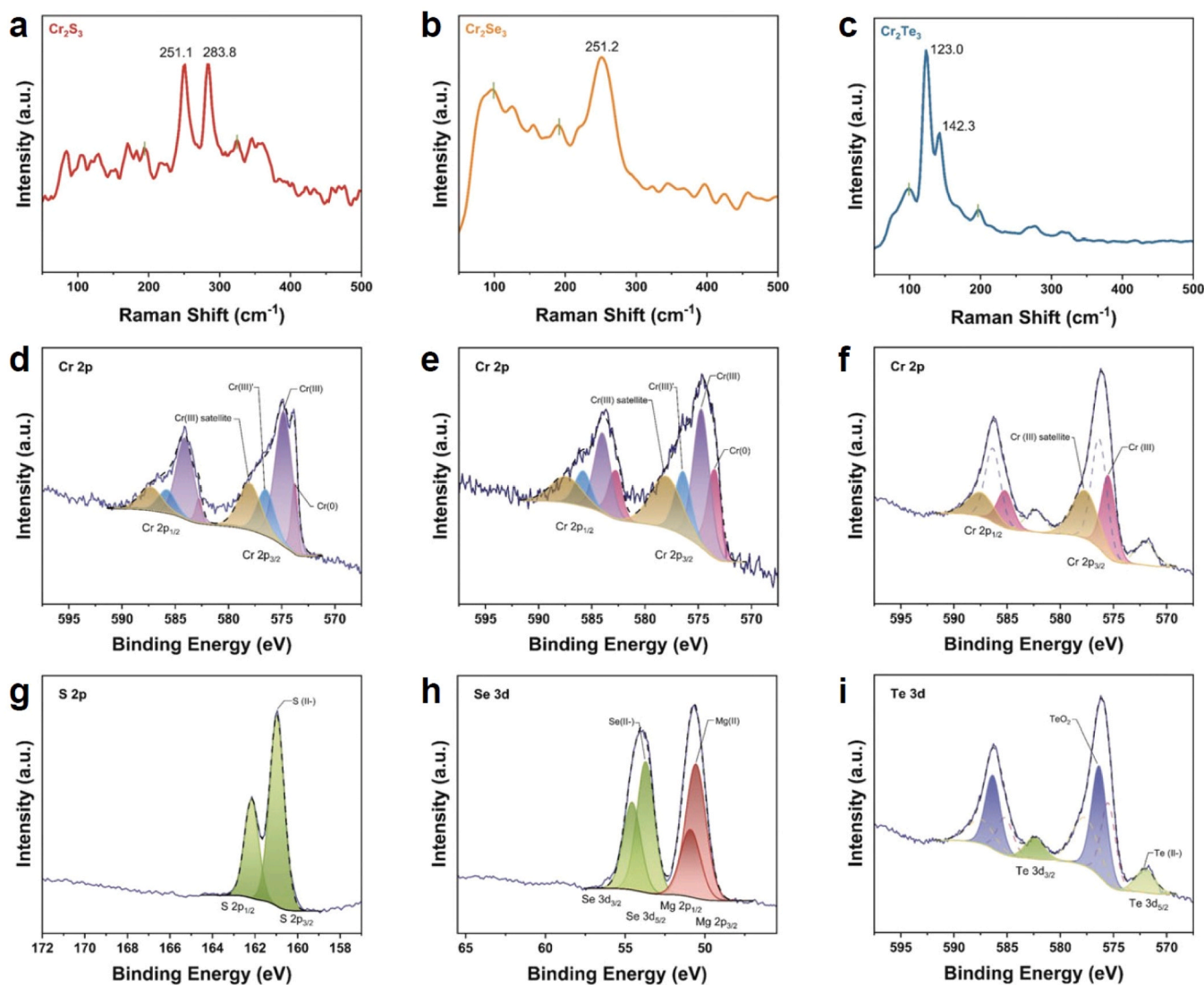


Fig. 2. Raman spectra of (a) Cr_2S_3 , (b) Cr_2Se_3 , and (c) Cr_2Te_3 nanosheets. XPS spectra showing the Cr 2p region of (d) Cr_2S_3 , (e) Cr_2Se_3 , and (f) Cr_2Te_3 nanosheets. XPS spectra showing the S 2p region of (g) Cr_2S_3 , the Se 3d region of (h) Cr_2Se_3 , and the Te 3d region of (i) Cr_2Te_3 nanosheets.

with extra Cr in between layers filling up 1/3 of the Cr positions [15], Cr_2X_3 is considered pseudo-layered due to the great 2D components. Therefore, the peak at 251.1 cm^{-1} was attributed to the in-plane Eg mode, and the other three peaks were associated with the out-of-plane Ag modes, consistent with previously reported values for Cr_2S_3 crystals [20–22]. Similarly, Cr_2Se_3 (Fig. 2b) exhibited a broad asymmetric band at about $100\text{--}200\text{ cm}^{-1}$ and a sharp peak at 251.2 cm^{-1} , corresponding to the in-plane Eg mode, which aligns with values reported for 2D Cr_2Se_3 nanosheets despite their different space groups [23]. The Raman peaks of Cr_2Te_3 (Fig. 2c) corroborated the composition, with two intense peaks at 123.0 cm^{-1} and 142.3 cm^{-1} , consistent with the extensive Raman characterization available for 2D Cr_2Te_3 of the same space group [24]. As a result, the stoichiometric ratio between metal and chalcogen in all the synthesized nanosheets was estimated to be 2:3.

To further confirm the compositional homogeneity of the as-synthesized samples, X-ray photoelectron spectroscopy (XPS) was conducted. After finishing the survey scans (Fig. S4) of three materials, narrow scans in the Cr 2p region were compared to obtain information about the compositions (Fig. 2d–f). In the analysis of the Cr 2p spectra, some chromium species can be represented by either multiplets or broad single peaks produced from the weighted average of the multiplets. As shown in Fig. 2d, Cr 2p_{3/2} could be fitted with a minor asymmetric peak at 573.7 eV, attributed to Cr^0 from metallic chromium, two peaks at 574.8 eV and 576.5 eV, attributed to Cr^{3+} from Cr_2S_3 and Cr_2O_3 respectively, [20,25–30] as well as the satellites of both Cr^{3+} peaks at higher binding energies (BEs) overlapping with one another, located at 578.0 eV. The corresponding Cr 2p^{1/2} components were identified based on the characteristic spin-orbit splitting of $9.3 \pm 0.2\text{ eV}$. According to Biesinger et al., the shake-up satellite for Cr^{3+} , which originates from reorganization of valence electrons after photoemission involving excitation to a higher unoccupied level, appear $\sim 5\text{ eV}$ after the main peak as a weak feature. [25] It is also plausible that the surface structures, which are dominant in 2D nanosheets, account for the satellite features in Cr 2p. The “surface peaks”, likely to be caused by the lack of coordination with cations and broken bonds at the surface, have been previously reported for compounds of the other transition metals. [31–33] Due to the difference in electronegativities, Cr 2p binding energies of Cr^{3+} from oxides are generally higher than that from the other chalcogenides. [25, 34] By comparing the peak areas after background subtraction, it can be observed that sulfide content outweighs that of the oxides. Notably, Cr^0 was likely formed when the introduced hydrogen inadvertently reduced the chromium chloride adatoms on the mica substrate, while chromium (III) oxide was formed after sample exposure to oxygen in atmospheric conditions. Similarly, Cr^0 peak at 573.4 eV, two Cr^{3+} peaks at 574.7 eV and 576.4 eV, and Cr^{3+} satellites at 578.0 eV are deconvoluted in Cr 2p^{3/2} region for Cr_2Se_3 (Fig. 2e). The assignment of the peak at 574.7 eV to Cr(III) selenide species agrees well with earlier reports. [27,35–37] For Cr_2Te_3 , due to the overlapping Cr 2p and Te 3d regions, only the intense Cr 2p^{3/2} peak from Cr_2Te_3 at 575.4 eV (Fig. 2f) can be distinguished, [38] whereas the one from Cr_2O_3 is masked by the strong Te 3d^{5/2} peak from TeO_2 at 576.3 eV, marked by the dotted line. The peak analysis of the Cr 2p and Te 3d spectra is done by introducing energy constraint for the different spin-orbit components, i.e., $\Delta\text{BE} \sim 9.3\text{ eV}$ for Cr 2p and $\Delta\text{BE} \sim 10.4\text{ eV}$ for Te 3d, and peak area constraint, i.e., 2:1 ratio for Cr 2p and 3:2 ratio for Te 3d. The Cr^{3+} satellite peaks at 577.3 eV are also fitted accordingly. Chalcogen narrow scans (Fig. 2g–i) further confirmed the chemical state of -2 for the relevant chalcogens: S 2p^{3/2} at 161.0 eV, [20,25,28] Se 3d^{5/2} at 53.7 eV, [27,35–37] and Te 3d^{5/2} at 572.1 eV. [35,38,39] As mentioned earlier, TeO_2 peak could also be fitted within the main peak illustrated in the Cr 2p region at 576.3 eV for 3d^{5/2}, [34,39,40] which again confirmed the occurrence of oxidation when the material was exposed to air. Nonetheless, XPS did not show the existence of chemical states other than $+3$ and 0 for Cr, supporting the conclusion that the as-synthesized Cr_2X_3 nanosheets are of homogeneous composition. The interference from oxidized and reduced Cr_2X_3 , likely to be surface species, was precluded for subsequent

characterization, as all remaining techniques were applied locally to selected single nanosheets. Notably, the peak pair appearing at around 51 eV is attributed to Mg^{2+} which comes from the F-mica substrate.

3.3. Structural analysis of the ultrathin chromium chalcogenides (Cr_2X_3)

Fig. 3a illustrates the crystal structure shared by the as-synthesized Cr_2X_3 nanosheets with *P*-31c (No.163) space group, in which the grey spheres represent chromium atoms while purple spheres represent chalcogen atoms. From the top view in the (001) plane, these atoms are arranged in three- or six-fold symmetry, consistent with the macroscopic triangular or hexagonal morphologies observed. Furthermore, from the side view in the (100) plane, Cr_2X_3 can be regarded as CrX_2 backbones with partially intercalated Cr atoms, terminating at chalcogen atoms in ideal cases. The high-angle annular dark-field scanning transmission electron microscopy (HAADF-STEM) images of Cr_2S_3 , Cr_2Se_3 , and Cr_2Te_3 (Fig. 3b–d Inset i) demonstrate the same atomic arrangement as the (001) plane of space group, and additional evidence from d-spacing analysis and fast Fourier transform (FFT) patterns were provided to determine the exact phase of as-grown Cr_2X_3 .

Beginning with Cr_2Te_3 , as it is thermodynamically stable only in the *P*-31c space group, the as-grown Cr_2Te_3 in our study also belongs to the same space group, supported by the similarity in synthesis parameters [12,17,18]. Furthermore, the (-120) and (110) lattice planes identified from the FFT pattern (inset) have a spacing of 3.4 \AA , half the length of the in-plane lattice parameter (*a* or *b*). This lead to an estimated in-plane lattice parameter of about 6.8 \AA , consistent with the theoretical value of 6.897 \AA [41] and the reported value of 6.82 \AA [42] for its bulk counterpart. Similarly, the lattice parameter estimated from Cr_2Se_3 (Fig. 3c) is about 6.4 \AA , in agreement with the theoretical value of 6.351 \AA [18] for the *P*-31c space group, confirming its crystal structure. Likewise, the calculated lattice constant for Cr_2S_3 is approximately 6.0 \AA , close to the 6.026 \AA [43] value reported for trigonal *P*-31c Cr_2S_3 . A closer examination of the FFT pattern (Fig. S5) reveals a smaller, dimmer set of spots with a six-fold symmetry, indicating the trigonal *P*-31c phase of the as-grown Cr_2S_3 [20].

Higher magnification HAADF-STEM images (Panel ii) exhibit a uniform distribution of chromium and chalcogen atoms for each composition. Notably, the contrast in HAADF-STEM images is determined by the atomic number, where atoms with higher atomic number (*Z* values) appear brighter. Consequently, chromium and relevant chalcogen atoms can be distinguished to reveal their detailed arrangement. In Cr_2S_3 , the brighter spots correspond to chromium atoms due to Cr's larger *Z* value than S, while in Cr_2Se_3 and Cr_2Te_3 , the brighter spots are attributed to the relevant chalcogen atoms. The overlaid schematics further illustrate the atomic arrangement, with grey spheres representing Cr, and yellow, orange, and blue spheres representing S, Se, and Te, respectively. Energy-dispersive X-ray spectroscopy (EDS) mapping in Inset iii (Fig. 3b–d) also confirms the uniform distribution of Cr and X atoms throughout all the nanosheets, supporting compositional homogeneity. The quantified analysis of EDS results in Fig. S6 indicates that the atomic ratio of Cr and X elements is approximately 2:3 for all three species, confirming the composition to be Cr_2X_3 . Additional support for compositional homogeneity and ratio is obtained from the quantified analysis of SEM-EDS results (Fig. S7).

3.4. Comparison of HER activities in chromium chalcogenides (Cr_2X_3)

The integration of single 2D nanoflakes into an on-chip microcell testing device provides a powerful platform to study a material's inherent catalytic activity, excluding interference from both testing environments, i.e., electrodes, and unexpected variables from catalysts, like facets and grain boundaries, since this setup enables accurate measurement within a restricted area of a pristine material [44]. To assess the catalytic properties of sample Cr_2X_3 nanosheets, only the basal area was isolated by creating a limited window of $10\text{ }\mu\text{m} \times 10\text{ }\mu\text{m}$ on a

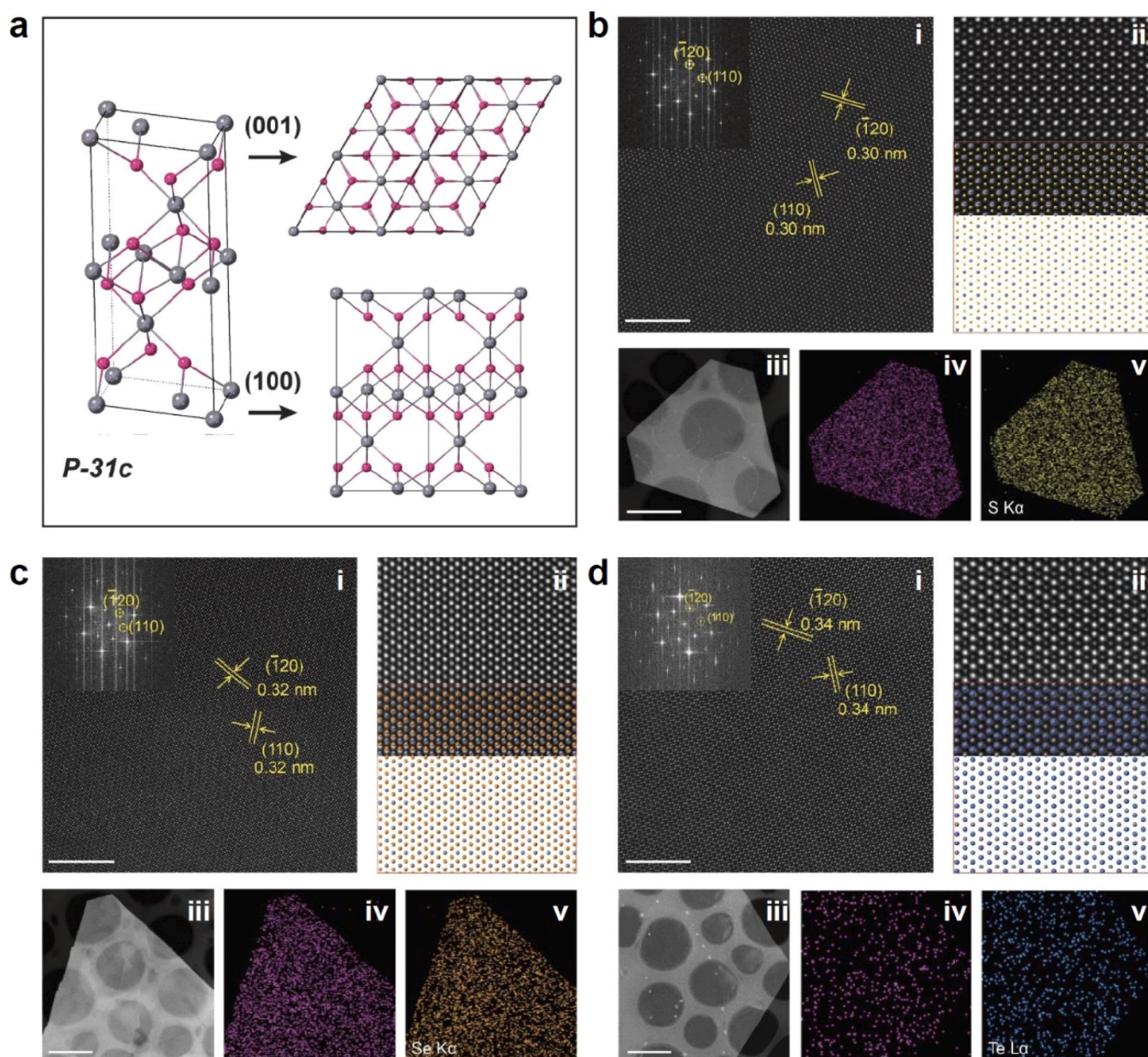


Fig. 3. (a) Illustration of the Cr₂X₃ crystal structure with atomic arrangement view from top and side. STEM characterizations of (b) Cr₂S₃, (c) Cr₂Se₃, and (d) Cr₂Te₃: (i) Large field-of-view HAADF-STEM image with FFT pattern shown in the inset. (ii) High resolution HAADF-STEM image overlaid with the atomic structure. (iii) EDX mapping. Scale bars: 5 nm (panel i) and 1 μm (panel iii).

single Cr₂X₃ nanosheet where the remaining area was passivated by PMMA layer (Fig. S8a) to eliminate the impact of edge area with different coordination conditions. The Cr₂X₃ nanosheets exhibited excellent stability during the electrocatalytic test in the reducing environment provided by the negative potential in the hydrogen evolution reaction (HER), as evidenced by the intact surface morphology (Fig. S8b).

Polarization curves of the 2D Cr₂X₃ nanosheets in the cathodic range revealed a decreasing trend in HER activity for Cr₂S₃, Cr₂Se₃, and Cr₂Te₃. The overpotentials required to achieve a current density reaches 10 mA cm⁻² increased from 147 mV for Cr₂S₃ to 202 mV for Cr₂Se₃ and 267 mV for Cr₂Te₃, while the current densities at -0.28 V vs RHE decreased from 60.3 mA cm⁻² for Cr₂S₃ to 40.1 mA cm⁻² for Cr₂Se₃ and 14.4 mA cm⁻² for Cr₂Te₃ (Fig. 4a). Despite the only difference being the chalcogen elements in the model materials, the HER activities varied considerably, with Cr₂S₃ exhibiting 1.5 times and 4.2 times higher

current densities than Cr₂Se₃ and Cr₂Te₃, respectively. To prove the covered region did not participate in the catalytic reaction, passivated region with PMMA was also tested under the same conditions. The grey dotted line (Fig. 4a) shows no change in current density throughout the entire scanning range, which indicates that the protected area did not respond to the changing potential, therefore supporting the reliability of the microelectronic setup.

The Tafel slopes extracted from the relevant HER regions demonstrated an improvement in reaction kinetics, with decreasing slopes from 176.9 mV dec⁻¹ for Cr₂S₃ to 137.3 mV dec⁻¹ for Cr₂Se₃ and 113.0 mV dec⁻¹ for Cr₂Te₃. However, as compared to the significant differences among their onset potentials, the improvement in Tafel slopes would not have much impact to the overall catalytic performance as observed in Fig. 4a. Nyquist plots of three candidates (Fig. 4c) show that Cr₂S₃ has a significantly improved faradaic impedance as compared to Cr₂Se₃ and Cr₂Te₃, as evident from the smaller plot shown in the inset. By analyzing

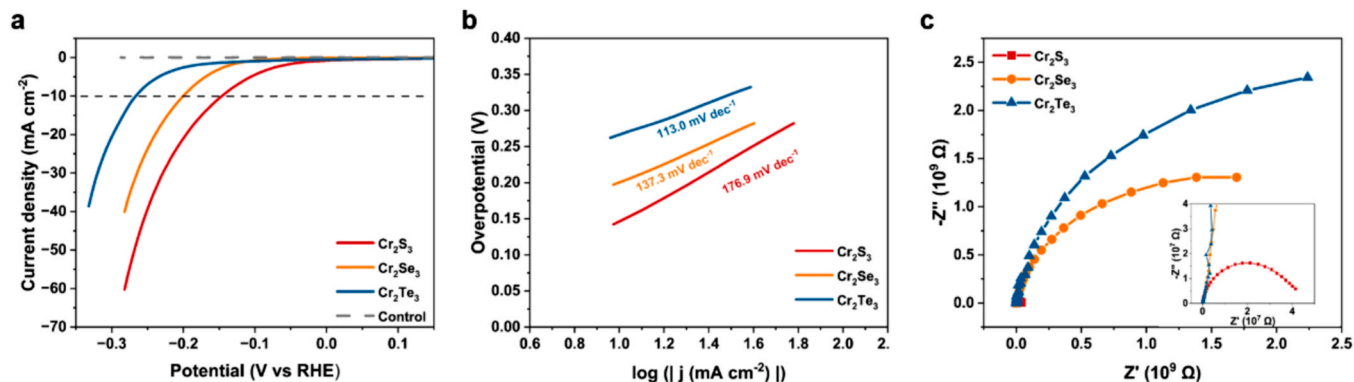


Fig. 4. (a) Polarization curves of basal planes for single Cr₂S₃, Cr₂Se₃, and Cr₂Te₃ nanosheets as well as the PMMA-passivated region, all normalized by the reaction area. (b) Tafel plots were derived according to the HER region in previous polarization curves. (c) Nyquist plots were obtained from EIS measurements of single Cr₂S₃, Cr₂Se₃, and Cr₂Te₃ nanosheets.

the semicircle features, the most significant component in the faradaic impedance, charge transfer resistance (R_{ct}) could be estimated [45] Cr₂S₃ has a two-order smaller R_{ct} of $3.92 \times 10^7 \Omega$ as compared to the $3.12 \times 10^9 \Omega$ of Cr₂Se₃ and $6.47 \times 10^9 \Omega$ of Cr₂Te₃, as shown in the equivalent circuit (Fig. S9).

3.5. Analysis of electrical properties of as-synthesized chromium chalcogenides

While previous reports indicate an enhancement in electrical conductivities from Cr₂S₃, to Cr₂Se₂ and Cr₂Te₃ nanoflakes, a more practical electrical transport property analysis was conducted on as-grown materials with physical dimensions close to those used in the electrocatalytic tests. Leveraging the planar morphology of 2D nanosheets, they were integrated into field-effect transistor (FET) devices to examine their electrical conductivities (Fig. S10).

In the I_{DS} - V_{DS} plots at various bottom gate voltages for the 8-nm thick Cr₂S₃ and Cr₂Se₃ (Fig. 5ab), typical p-type semiconductor characteristics were observed, with improved electrical conductivities as negative gate voltage was applied in the channel. A consistent increasing trend of conductivities was observed with negative gate voltage decreasing from 0 to -60 V for both Cr₂S₃ and Cr₂Se₃. However, the Cr₂Te₃ nanosheet displayed a characteristic metallic nature, as conductivities remained unchanged despite varying gate voltages (Fig. 5c).

From the I_{DS} - V_{DS} plots in the insets, the I_0 values at $V_G = 0$ V and $V_{DS} = 5$ V were extracted to be approximately 0.175 nA, 183 nA, and 4.96×10^5 nA for Cr₂S₃, Cr₂Se₃, and Cr₂Te₃, respectively, all of similar dimensions. The hole mobilities of the 8-nm thick 2D Cr₂S₃ and Cr₂Se₃ were also estimated to be $1.91 \times 10^{-3} \text{ cm}^2 \text{ V}^{-1} \text{ s}^{-1}$ and $2.02 \times 10^{-2} \text{ cm}^2 \text{ V}^{-1} \text{ s}^{-1}$ (Details showed in SI), which aligns with the observed positive conductivity trend. From the electrical property characterization results,

an anomalous rivalry is observed considering the decreasing trend in catalytic performance from Cr₂S₃ to Cr₂Se₃, and eventually Cr₂Te₃.

3.6. Analysis based on intrinsic HER activities of Cr₂S₃, Cr₂Se₃, and Cr₂Te₃ via density functional theory (DFT) calculation

DFT calculation based on Cr₂S₃, Cr₂Se₃, and Cr₂Te₃ was conducted to further prove the intrinsic catalytic activity is predominant in determining the HER performance in this material class. Same (001) surfaces were chosen in the calculation since macroscopically triangular or hexagonal Cr₂X₃ nanosheets of all three species only expose the (001) facet owing to their planar nature. The absorption of proton, represented by tiny pink spheres, is illustrated in both the side and top views of the atomic structures (Fig. 6a-c). For each Cr₂X₃(001) surface, all three kinds of adsorption locations, top, hollow and bridge sites, are explored initially. During the optimization process, our simulation indicated that *H in the hollow and bridge sites would eventually transform to the top sites as marked by the red circles in the top views of the (001) surfaces, demonstrating that top sides would provide the optimal adsorption condition to protons for all three Cr₂X₃ species. Meanwhile, the same adsorption locations precluded interferences from varied coordination conditions, therefore also proving Cr₂X₃ reliable model materials for performance comparison and benchmarking. The calculated local density of states (LDOS) in the surface atoms (Fig. S12) suggested both Cr₂S₃ (100) and Cr₂Se₃(100) facets are desired to harbor protons since they both have strong peaks near the Fermi energy level, indicating the good capabilities of material surfaces to accumulate electrons, which facilitates the subsequent bond formation with the incoming substances [46,47]. However, the peak intensity around the Fermi level is weaker for the Cr₂Te₃(001) surface, indicating its active sites' poorer ability to trap protons, as evidenced by the much higher onset potential in previous

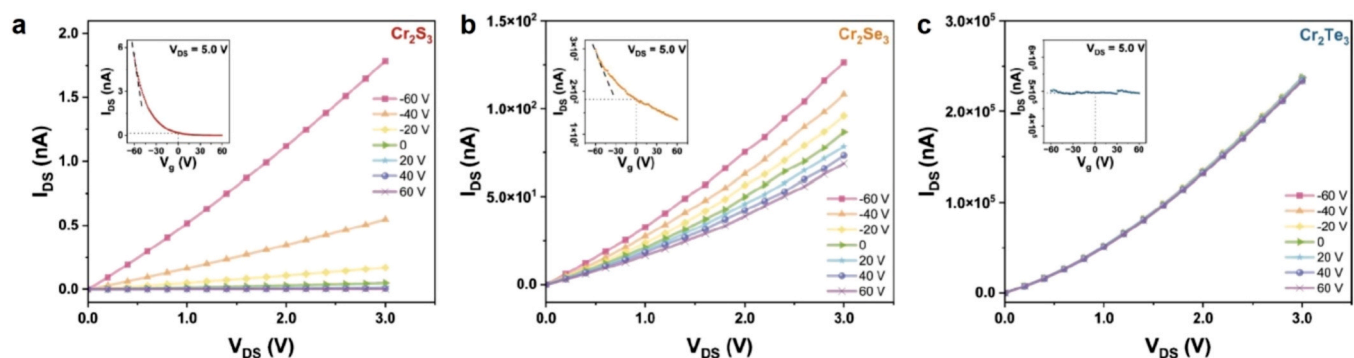


Fig. 5. I_{DS} - V_{DS} plots of FET devices fabricated based on (a) Cr₂S₃, (b) Cr₂Se₃, and (c) Cr₂Te₃ single flake with insets portraying I_{DS} - V_G characteristics at constant V_{DS} of 5 V.

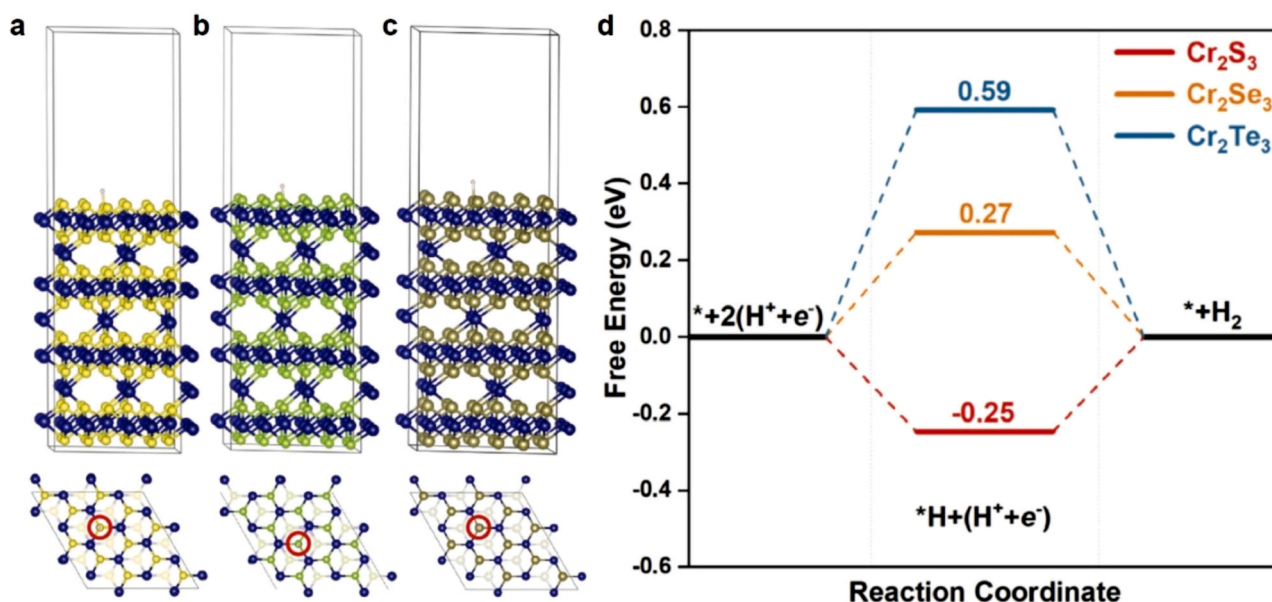


Fig. 6. Side and top view atomic structures of H^+ adsorbed on the (a) $\text{Cr}_2\text{S}_3(001)$, (b) $\text{Cr}_2\text{Se}_3(001)$, and (c) $\text{Cr}_2\text{Te}_3(001)$ surfaces. (d) Gibbs free energy change along HER on $\text{Cr}_2\text{S}_3(001)$, $\text{Cr}_2\text{Se}_3(001)$, and $\text{Cr}_2\text{Te}_3(001)$ surfaces. The free energy change of an ideal catalyst should be close to 0. The blue, yellow, green, and brown spheres indicate Cr, S, Se, and Te atoms, respectively.

electrocatalytic performance characterization.

Furthermore, the intrinsic HER catalytic activities of $\text{Cr}_2\text{S}_3(001)$, $\text{Cr}_2\text{Se}_3(001)$, and $\text{Cr}_2\text{Te}_3(001)$ surfaces were theoretically evaluated based on the DFT calculation. Notably, the desorption step used in our calculation is presumed to proceed through the Heyrovsky mechanism owing to the low Hads coverage calculated in previous DFT calculations reported for 1 T-MoS2 with the similar surface structure [48]. Ideally, the free energy change of an ideal catalyst for HER is almost zero according to the previous research [49]. However, the free energy barriers of HER on the $\text{Cr}_2\text{S}_3(001)$, $\text{Cr}_2\text{Se}_3(001)$, and $\text{Cr}_2\text{Te}_3(001)$ surfaces are calculated to be 0.25, 0.27, and 0.59 eV, respectively, suggesting a decreasing trend of intrinsic HER catalytic activities, which are in good agreement with the experimental catalytic performances. Moreover, these plots along reaction coordinate also indicate the rate determining step for Cr_2S_3 is the H_2 generation-desorption process, which is consistent with the poorer reaction kinetics as evidenced by the steep Tafel slope since the challenging generation-desorption process leads to fewer available active sites and thus hinders the subsequent proton adsorption.

Despite the small difference between the absolute value of ΔG_{H} for $\text{Cr}_2\text{S}_3(001)$ and $\text{Cr}_2\text{Se}_3(001)$ of 0.02 eV, the exchange current density for $\text{Cr}_2\text{S}_3(001)$ was estimated to be about 1.6 times of $\text{Cr}_2\text{Se}_3(001)$ based on the logarithmic scale in the theoretically derived volcano plot against ΔG_{H} [50]. For $\text{Cr}_2\text{S}_3(001)$ and $\text{Cr}_2\text{Se}_3(001)$ with identical atomic arrangement, it also indicates that the intrinsic HER activity of $\text{Cr}_2\text{S}_3(001)$ is equivalently about 1.6 times as high as that of $\text{Cr}_2\text{Se}_3(001)$. The experimental catalytic performances of Cr_2S_3 and Cr_2Se_3 in Fig. 3a present a similar trend regardless of the deteriorating electrical conductivities, supporting the intrinsic catalytic activity, comparing to the electrical transport properties, are the more dominating factor in determining catalytic performances in this material class.

4. Conclusion

In summary, we successfully synthesized 2D Cr_2X_3 ($\text{X} = \text{S}, \text{Se}, \text{Te}$) nanosheets with ultrathin thickness and consistent crystal structures using a simple ambient pressure chemical vapor deposition method. These nanosheets exhibit single crystallinity, good chemical homogeneity, and desired surface topology, making them ideal models for comparing catalytic performances. For nanosheets with a thickness of

around 8 nm, we observed a decreasing trend in HER activities in acidic media from Cr_2S_3 to Cr_2Se_3 , and finally Cr_2Te_3 , with increasing overpotentials of 147 mV, 202 mV, and 267 mV at a current density of 10 mA cm^{-2} , respectively. Similarly, the current densities at an overpotential of 0.28 V decreased from 60.3 mA cm^{-2} to 40.1 mA cm^{-2} , and 14.4 mA cm^{-2} for Cr_2S_3 , Cr_2Se_3 , and Cr_2Te_3 , respectively. Conversely, the electrical transport properties exhibited an opposite trend, with Cr_2Te_3 displaying metallic behavior and Cr_2S_3 and Cr_2Se_3 behaving as p-type semiconductors. The increasing currents extracted from $I_{\text{DS}}-V_{\text{G}}$ tests for MOSFET devices (0.175 nA , 183 nA , and $4.96 \times 10^5 \text{ nA}$) for Cr_2S_3 , Cr_2Se_3 , and Cr_2Te_3 , respectively, also support this trend. The observed increase in hole mobilities for Cr_2S_3 and Cr_2Se_3 further confirms this trend in electrical properties. In-depth DFT calculations provided valuable insights into the opposing trend between HER performance and electrical properties, suggesting that intrinsic catalytic activities play a more dominant role in determining overall catalytic performance compared to electrical properties. These findings serve as an inspiration for future research, emphasizing the significance of intrinsic catalytic activity when designing and selecting electrocatalysts, particularly within the domain of 2D materials.

CRedit authorship contribution statement

Jiefu Yang: Conceptualization, Methodology, Investigation, Writing-original draft. **Mei Zheng:** Methodology, Investigation, Software, Validation. **Yao Wu:** Methodology, Investigation, Writing-editing. **Frédéric Le Goulher:** Investigation, Data analysis, Writing-editing. **Jun Di:** Validation, Revising. **Teddy Salim:** Methods, Data Analysis, Validation. **Ya Deng:** Revising. **Chao Zhu:** Methodology **Shasha Guo:** Methodology. **Bijun Tang:** Revising. **Shuzhou Li:** Software, Validation, Supervision. **Zheng Liu:** Conceptualization, Supervision, Writing-reviewing & editing, Project administration, Funding acquisition.

Declaration of Competing Interest

The authors declare that they have no known competing financial interests or personal relationships that could have appeared to influence the work reported in this paper.

Data Availability

Data will be made available on request.

Acknowledgments

This work was supported by the Singapore Ministry of Education AcRF Tier 2 (MOE2019-T2-2-105), AcRF Tier 1 RG4/17, and RG161/19. Y.W. acknowledges the Facility for Analysis, Characterization, Testing, and Simulation (FACTS), Nanyang Technological University, Singapore for the use of their electron microscopy facility. Z.M. and L. SZ. acknowledges the computing resources from National Supercomputing Centre Singapore (NSCC).

Appendix A. Supporting information

Supplementary data associated with this article can be found in the online version at [doi:10.1016/j.apcatb.2023.123478](https://doi.org/10.1016/j.apcatb.2023.123478).

References

- [1] Y. Xiao, C.W. Lim, J. Chang, Q. Yuan, L. Wang, N. Yan, Electrocatalytic amino acid synthesis from biomass-derivable keto acids over ball milled carbon nanotubes, *Green. Chem.* 25 (2023) 3117–3126, <https://doi.org/10.1039/D3GC00265A>.
- [2] S. Wang, A. Lu, C.-J. Zhong, Hydrogen production from water electrolysis: role of catalysts, *Nano Converg.* 8 (2021), 4, <https://doi.org/10.1186/s40580-021-00254-x>.
- [3] N.-T. Suen, S.-F. Hung, Q. Quan, N. Zhang, Y.-J. Xu, H.M. Chen, Electrocatalysis for the oxygen evolution reaction: recent development and future perspectives, *Chem. Soc. Rev.* 46 (2017) 337–365, <https://doi.org/10.1039/C6CS00328A>.
- [4] A. Kostuch, S. Jarczewski, M.K. Surówka, P. Kuśrowski, Z. Sojka, K. Kruczała, The joint effect of electrical conductivity and surface oxygen functionalities of carbon supports on the oxygen reduction reaction studied over bare supports and Mn–Co spinel/carbon catalysts in alkaline media, *Catal. Sci. Technol.* 11 (2021) 7578–7591, <https://doi.org/10.1039/D1CY01115D>.
- [5] Y. Yang, Y. Yu, J. Li, Q. Chen, Y. Du, P. Rao, R. Li, C. Jia, Z. Kang, P. Deng, Y. Shen, X. Tian, Engineering ruthenium-based electrocatalysts for effective hydrogen evolution reaction, *Nano-Micro Lett.* 13 (2021), 160, <https://doi.org/10.1007/s40820-021-00679-3>.
- [6] Y. Yan, C. Wang, Z. Huang, J. Fu, Z. Lin, X. Zhang, J. Ma, J. Shen, Highly efficient and robust catalysts for the hydrogen evolution reaction by surface nano engineering of metallic glass, *J. Mater. Chem. A* 9 (2021) 5415–5424, <https://doi.org/10.1039/D0TA10235K>.
- [7] J. Zhou, J. Lin, X. Huang, Y. Zhou, Y. Chen, J. Xia, H. Wang, Y. Xie, H. Yu, J. Lei, D. Wu, F. Liu, Q. Fu, Q. Zeng, C.-H. Hsu, C. Yang, L. Lu, T. Yu, Z. Shen, H. Lin, B. I. Yakobson, Q. Liu, K. Suenaga, G. Liu, Z. Liu, A library of atomically thin metal chalcogenides, *Nature* 556 (2018) 355–359, <https://doi.org/10.1038/s41586-018-0008-3>.
- [8] G. Kresse, J. Furthmüller, Efficient iterative schemes for ab initio total-energy calculations using a plane-wave basis set, *Phys. Rev. B* 54 (1996) 11169–11186, <https://doi.org/10.1103/PhysRevB.54.11169>.
- [9] G. Kresse, D. Joubert, From ultrasoft pseudopotentials to the projector augmented-wave method, *Phys. Rev. B* 59 (1999) 1758–1775, <https://doi.org/10.1103/PhysRevB.59.1758>.
- [10] P.E. Blöchl, Projector augmented-wave method, *Phys. Rev. B* 50 (1994) 17953–17979, <https://doi.org/10.1103/PhysRevB.50.17953>.
- [11] J.P. Perdew, K. Burke, M. Ernzerhof, Generalized gradient approximation made simple, *Phys. Rev. Lett.* 77 (1996) 3865–3868, <https://doi.org/10.1103/PhysRevLett.77.3865>.
- [12] H.J. Monkhorst, J.D. Pack, Special points for Brillouin-zone integrations, *Phys. Rev. B* 13 (1976) 5188–5192, <https://doi.org/10.1103/PhysRevB.13.5188>.
- [13] S. Grimme, Semiempirical GGA-type density functional constructed with a long-range dispersion correction, *J. Comput. Chem.* 27 (2006) 1787–1799, <https://doi.org/10.1002/jcc.20495>.
- [14] A.A. Peterson, F. Abild-Pedersen, F. Studt, J. Rossmeisl, J.K. Nørskov, How copper catalyzes the electroreduction of carbon dioxide into hydrocarbon fuels, *Energy Environ. Sci.* 3 (2010) 1311, <https://doi.org/10.1039/c0ee00071j>.
- [15] D. Pradhan, A. Gartia, S.P. Ghosh, K.K. Sahoo, G. Bose, J.P. Kar, Impact of H₂ gas on the properties of MoS₂ thin films deposited by sulfurization of Mo thin films, *Micro & Nano Lett.* 16 (2021) 525–532, <https://doi.org/10.1049/mna2.12058>.
- [16] R. Cheng, L. Yin, Y. Wen, B. Zhai, Y. Guo, Z. Zhang, W. Liao, W. Xiong, H. Wang, S. Yuan, J. Jiang, C. Liu, J. He, Ultrathin ferrite nanosheets for room-temperature two-dimensional magnetic semiconductors, *Nat. Commun.* 13 (2022), 5241, <https://doi.org/10.1038/s41467-022-33017-1>.
- [17] J. Chu, Y. Zhang, Y. Wen, R. Qiao, C. Wu, P. He, L. Yin, R. Cheng, F. Wang, Z. Wang, J. Xiong, Y. Li, J. He, Sub-millimeter-scale growth of one-unit-cell-thick ferrimagnetic Cr₂S₃ nanosheets, *Nano Lett.* 19 (2019) 2154–2161, <https://doi.org/10.1021/acs.nanolett.9b00386>.
- [18] M. Chevreton, B. Dumont, Chimie minérale. Etude structurale de nouveaux seleniures de chrome Cr₂Se₃, *Comptes Rendus Hebdomadaires Des Seances de l'Academie Des Sciences, Serie C, Sciences Chimiques* (1966–). 267 (1968) 884–887.
- [19] M. Bian, A.N. Kamenskii, M. Han, W. Li, S. Wei, X. Tian, D.B. Eason, F. Sun, K. He, H. Hui, F. Yao, R. Sabirianov, J.P. Bird, C. Yang, J. Miao, J. Lin, S.A. Crooker, Y. Hou, H. Zeng, Covalent 2D Cr₂Te₃ ferromagnet, *Mater. Res. Lett.* 9 (2021) 205–212, <https://doi.org/10.1080/21663831.2020.1865469>.
- [20] F. Cui, X. Zhao, J. Xu, B. Tang, Q. Shang, J. Shi, Y. Huan, J. Liao, Q. Chen, Y. Hou, Q. Zhang, S.J. Pennycook, Y. Zhang, Controlled growth and thickness-dependent conduction-type transition of 2D ferrimagnetic Cr₂S₃ semiconductors, *Adv. Mater.* 32 (2020), 1905896, <https://doi.org/10.1002/adma.201905896>.
- [21] W. Hussain, A. Badshah, R.A. Hussain, Imtiaz-ud-Din, M.A. Aleem, A. Bahadur, S. Iqbal, M.U. Farooq, H. Ali, Photocatalytic applications of Cr₂S₃ synthesized from single and multi-source precursors, *Mater. Chem. Phys.* 194 (2017) 345–355, <https://doi.org/10.1016/j.matchemphys.2017.04.001>.
- [22] C. Avril, V. Malavergne, R. Caracas, B. Zanda, B. Reynard, E. Charon, E. Bobocioiu, F. Brunet, S. Borensztajn, S. Pont, M. Tarrida, F. Guyot, Raman spectroscopic properties and Raman identification of CaS-MgS-MnS-FeS-Cr₂FeS₄ sulfides in meteorites and reduced sulfur-rich systems, *Meteor. Planet. Sci.* 48 (2013) 1415–1426, <https://doi.org/10.1111/maps.12145>.
- [23] D. Zhang, C. Yi, C. Ge, W. Shu, B. Li, X. Duan, A. Pan, X. Wang, Controlled vapor growth of 2D magnetic Cr₂Se₃ and its magnetic proximity effect in heterostructures, *Chin. Phys. B* 30 (2021), 097601, <https://doi.org/10.1088/1674-1056/ac0cd9>.
- [24] J. Zhong, M. Wang, T. Liu, Y. Zhao, X. Xu, S. Zhou, J. Han, L. Gan, T. Zhai, Strain-sensitive ferromagnetic two-dimensional Cr₂Te₃, *Nano Res.* 15 (2022) 1254–1259, <https://doi.org/10.1007/s12274-021-3633-3>.
- [25] M.C. Biesinger, C. Brown, J.R. Mycroft, R.D. Davidson, N.S. McIntyre, X-ray photoelectron spectroscopy studies of chromium compounds, *Surf. Interface Anal.* 36 (2004) 1550–1563, <https://doi.org/10.1002/sia.1983>.
- [26] M.C. Biesinger, B.P. Payne, A.P. Grosvenor, L.W.M. Lau, A.R. Gerson, R.St. C. Smart, Resolving surface chemical states in XPS analysis of first row transition metals, oxides and hydroxides: Cr, Mn, Fe, Co and Ni, *Appl. Surf. Sci.* 257 (2011) 2717–2730, <https://doi.org/10.1016/j.apusc.2010.10.051>.
- [27] E. Agostinelli, C. Battistoni, D. Fiorani, G. Mattogno, M. Nogue, An XPS study of the electronic structure of the ZnxCd1-xCr₂(X = S, Se) spinel system, *J. Phys. Chem. Solids* 50 (1989) 269–272, [https://doi.org/10.1016/0022-3697\(89\)90487-3](https://doi.org/10.1016/0022-3697(89)90487-3).
- [28] M.R. Habib, S. Wang, W. Wang, H. Xiao, S.M. Obaidulla, A. Gayen, Y. Khan, H. Chen, M. Xu, Electronic properties of polymorphic two-dimensional layered chromium disulphide, *Nanoscale* 11 (2019) 20123–20132, <https://doi.org/10.1039/C9NR04449C>.
- [29] I. Ikemoto, K. Ishii, S. Kinoshita, H. Kuroda, M.A. Alario Franco, J.M. Thomas, X-ray photoelectron spectroscopic studies of CrO₂ and some related chromium compounds, *J. Solid State Chem.* 17 (1976) 425–430, [https://doi.org/10.1016/S0022-4596\(76\)80012-6](https://doi.org/10.1016/S0022-4596(76)80012-6).
- [30] A. Kadari, T. Schemme, D. Kadri, J. Wollschläger, XPS and morphological properties of Cr₂O₃ thin films grown by thermal evaporation method, *Results Phys.* 7 (2017) 3124–3129, <https://doi.org/10.1016/j.rinp.2017.08.036>.
- [31] A.P. Grosvenor, B.A. Kobe, M.C. Biesinger, N.S. McIntyre, Investigation of multiplet splitting of Fe 2p XPS spectra and bonding in iron compounds, *Surf. Interface Anal.* 36 (2004) 1564–1574, <https://doi.org/10.1002/sia.1984>.
- [32] A.P. Grosvenor, M.C. Biesinger, R.St.C. Smart, N.S. McIntyre, New interpretations of XPS spectra of nickel metal and oxides, *Surf. Sci.* 600 (2006) 1771–1779, <https://doi.org/10.1016/j.susc.2006.01.041>.
- [33] A. Jaiswal, R. Das, K. Vivekanand, P. Mary Abraham, S. Adyanthaya, P. Poddar, Effect of Reduced Particle Size on the Magnetic Properties of Chemically Synthesized BiFeO₃ Nanocrystals, *J. Phys. Chem. C* 114 (2010) 2108–2115, <https://doi.org/10.1021/jp910745g>.
- [34] A. Shivayogimath, J.D. Thomsen, D.M.A. Mackenzie, M. Geisler, R.-M. Stan, A. J. Holt, M. Bianchi, A. Crovetto, P.R. Whelan, A. Carvalho, A.H.C. Neto, P. Hofmann, N. Stenger, P. Bøggild, T.J. Booth, A universal approach for the synthesis of two-dimensional binary compounds, *Nat. Commun.* 10 (2019), 2957, <https://doi.org/10.1038/s41467-019-1075-2>.
- [35] A.-T. Buruiana, F. Sava, N. Iacob, E. Matei, A.E. Bocirnea, M. Onea, A.-C. Galca, C. Mihai, A. Velea, V. Kuncser, Micrometer Sized Hexagonal Chromium Selenide Flakes for Cryogenic Temperature Sensors, *Sensors* 21 (2021) 8084, <https://doi.org/10.3390/s21238084>.
- [36] A. Roy, R. Dey, T. Pramanik, A. Rai, R. Schalip, S. Majumder, S. Guchhait, S. K. Banerjee, Structural and magnetic properties of molecular beam epitaxy grown chromium selenide thin films, *Phys. Rev. Mater.* 4 (2020), 025001, <https://doi.org/10.1103/PhysRevMaterials.4.025001>.
- [37] S.-J. Zhang, J.-M. Yan, F. Tang, J. Wu, W.-Q. Dong, D.-W. Zhang, F.-S. Luo, L. Chen, Y. Fang, T. Zhang, Y. Chai, W. Zhao, X. Wang, R.-K. Zheng, Colossal Magnetoresistance in Ti Lightly Doped Cr₂Se₃ Single Crystals with a Layered Structure, *ACS Appl. Mater. Interfaces* 13 (2021) 58949–58955, <https://doi.org/10.1021/acsami.1c18848>.
- [38] B. Xia, K. Long, X. Peng, Y. Ge, X. Liang, D. Gao, Asynchronous strategy in the nucleation of Cr₂Te₃@FeTe Heterolayers: Synthesis and magnetic behaviors, *J. Magn. Magn. Mater.* 579 (2023), 170875, <https://doi.org/10.1016/j.jmmm.2023.170875>.
- [39] D. Telesca, Y. Nie, J.I. Budnick, B.O. Wells, B. Sinkovic, Impact of valence states on the superconductivity of iron telluride and iron selenide films with incorporated oxygen, *Phys. Rev. B* 85 (2012), 214517, <https://doi.org/10.1103/PhysRevB.85.214517>.

- [40] K.-T. Chen, D.T. Shi, H. Chen, B. Granderson, M.A. George, W.E. Collins, A. Burger, R.B. James, Study of oxidized cadmium zinc telluride surfaces, *J. Vac. Sci. Technol. A: Vac., Surf., Films* 15 (1997) 850–853, <https://doi.org/10.1116/1.580719>.
- [41] The Materials Project, Materials Data on Cr₂Te₃ by Materials Project, (2020). <https://doi.org/10.17188/1201718>.
- [42] T. Hamasaki, T. Hashimoto, Y. Yamaguchi, H. Watanabe, Neutron diffraction study of Cr₂Te₃ single crystal, *Solid State Commun.* 16 (1975) 895–897, [https://doi.org/10.1016/0038-1098\(75\)90888-1](https://doi.org/10.1016/0038-1098(75)90888-1).
- [43] The Materials Project, Materials Data on Cr₂S₃ by Materials Project, (2020). <https://doi.org/10.17188/1268882>.
- [44] M. Ding, Q. He, G. Wang, H.-C. Cheng, Y. Huang, X. Duan, An on-chip electrical transport spectroscopy approach for in situ monitoring electrochemical interfaces, *Nat. Commun.* 6 (2015), 7867, <https://doi.org/10.1038/ncomms8867>.
- [45] A. Lasia, Mechanism and kinetics of the hydrogen evolution reaction, *Int. J. Hydrog. Energy* 44 (2019) 19484–19518, <https://doi.org/10.1016/j.ijhydene.2019.05.183>.
- [46] M. Zheng, Y. Li, K. Ding, Y. Zhang, W. Chen, W. Lin, Nitrogen fixation on metal-free SiC(111) polar surfaces, *J. Mater. Chem. A* 8 (2020) 7412–7421, <https://doi.org/10.1039/D0TA00981D>.
- [47] Z. Chen, J. Zhao, L. Yin, Z. Chen, B-terminated (111) polar surfaces of BP and BAs: promising metal-free electrocatalysts with large reaction regions for nitrogen fixation, *J. Mater. Chem. A* 7 (2019) 13284–13292, <https://doi.org/10.1039/C9TA01410A>.
- [48] Q. Tang, D. Jiang, Mechanism of hydrogen evolution reaction on 1T-MoS₂ from first principles, *ACS Catal.* 6 (2016) 4953–4961, <https://doi.org/10.1021/acscatal.6b01211>.
- [49] C. Liu, Q. Li, C. Wu, J. Zhang, Y. Jin, D.R. MacFarlane, C. Sun, Single-boron catalysts for nitrogen reduction reaction, *J. Am. Chem. Soc.* 141 (2019) 2884–2888, <https://doi.org/10.1021/jacs.8b13165>.
- [50] J. Ekspong, E. Gracia-Espino, T. Wågberg, Hydrogen evolution reaction activity of heterogeneous materials: a theoretical model, *J. Phys. Chem. C* 124 (2020) 20911–20921, <https://doi.org/10.1021/acs.jpcc.0c05243>.